# Role of multiaxial stress state in the hydrogen-assisted rolling-contact fatigue in bearings for wind turbines

J. Toribio, M. Lorenzo, D. Vergara
*Fracture of Materials and Structural Integrity Research Group, University of Salamanca, Spain*
*toribio@usal.es, mlorenzo@usal.es, dvergara@usal.es*

**ABSTRACT.** Offshore wind turbines often involve important engineering challenges such as the improvement of hydrogen embrittlement resistance of the turbine bearings. These elements frequently suffer the so-called phenomenon of hydrogen-assisted rolling-contact fatigue (HA-RCF) as a consequence of the synergic action of the surrounding harsh environment (the lubricant) supplying hydrogen to the material and the cyclic multiaxial stress state caused by in-service mechanical loading. Thus the complex phenomenon could be classified as hydrogen-assisted rolling-contact multiaxial fatigue (HA-RC-MF). This paper analyses, from the mechanical and the chemical points of view, the so-called ball-on-rod test, widely used to evaluate the hydrogen embrittlement susceptibility of turbine bearings. Both the stress-strain states and the steady-state hydrogen concentration distribution are studied, so that a better elucidation can be obtained of the potential fracture places where the hydrogen could be more harmful and, consequently, where the turbine bearings could fail during their life in service.

**KEYWORDS.** Hydrogen-assisted rolling-contact multiaxial fatigue; Wind turbines; bearings; Numerical analysis.

## INTRODUCTION

Offshore wind turbines often involve important engineering challenges [1], one of the most important being the improvement of hydrogen embrittlement resistance of the turbine bearings, a key issue in the evaluation of the structural integrity of such components. These elements are prone to suffer the so-called phenomenon of hydrogen-assisted rolling-contact fatigue (HA-RCF) [2, 3] as a consequence of the synergic action of the surrounding harsh environment (the lubricant) supplying hydrogen to the material and the cyclic multiaxial stress state caused by in-service mechanical loading [2, 3]. Thus the complex phenomenon of progressive damage could be classified as hydrogen-assisted rolling-contact multiaxial fatigue (HA-RC-MF).

Three important aspects linked with bearing failures are being extensively researched: (i) rolling contact fatigue (RCF) [4-7], (ii) influence of carbide particles on fatigue life [8,9], and (iii) local microplastic strain accumulation via ratcheting [10-12]. To achieve a better assessment of the structural integrity of such components, the analysis of hydrogen accumulation (revealing the prospective damage places) arises as a key issue. In previous studies [2, 3], the widely used RC-MF *ball-on-rod* test [12-15] was simulated by the finite element method (FEM) in order to obtain the stress-strain state inside the bearings during life in-service. From these states, the hydrogen distribution corresponding to the steady-state in the radial direction of the bearing was obtained. This paper goes further in the study developed in previous research [2, 3] including the analysis of the hydrogen distributions in hoop and axial directions, in order to obtain the potential fracture places where the hydrogen embrittlement phenomenon initiates.

## NUMERICAL MODELING

The study was divided into two uncoupled analysis. On one hand, the numerical simulation by means of a commercial finite element (FE) code was used for obtaining the stress and strain states after six revolutions of the bar. From the results of such an analysis, a simple estimation of the hydrogen accumulation for long time of exposure to hydrogenating environment was carried out allowing the estimation of the potential hydrogen damage places.
The geometry analysed consist in a steel bar of length $L$= 6 mm and diameter $d$ = 9.53 mm which rotates in contact with three equidistant steel balls of diameter $D$ = 12.70 mm which apply a point load of $F$ = 300 N over the bar surface as reflects the scheme of Fig. 1a. The complete 3D geometry can be simplified to a half just considering the symmetry plane $r$-θ shown in Fig. 1b and applying the corresponding boundary conditions as restricted displacement on the bar axial direction for all the nodes placed inside the symmetry plane. Thus, an important save of computing time is achieved optimizing the available resources. In addition, the geometry of the contacting balls can be also simplified considering the symmetry plane $r$-$z$ of such components. Taking this into account, only a quarter of the whole geometry of the ball is modelled, as can be seen in Fig. 1b.

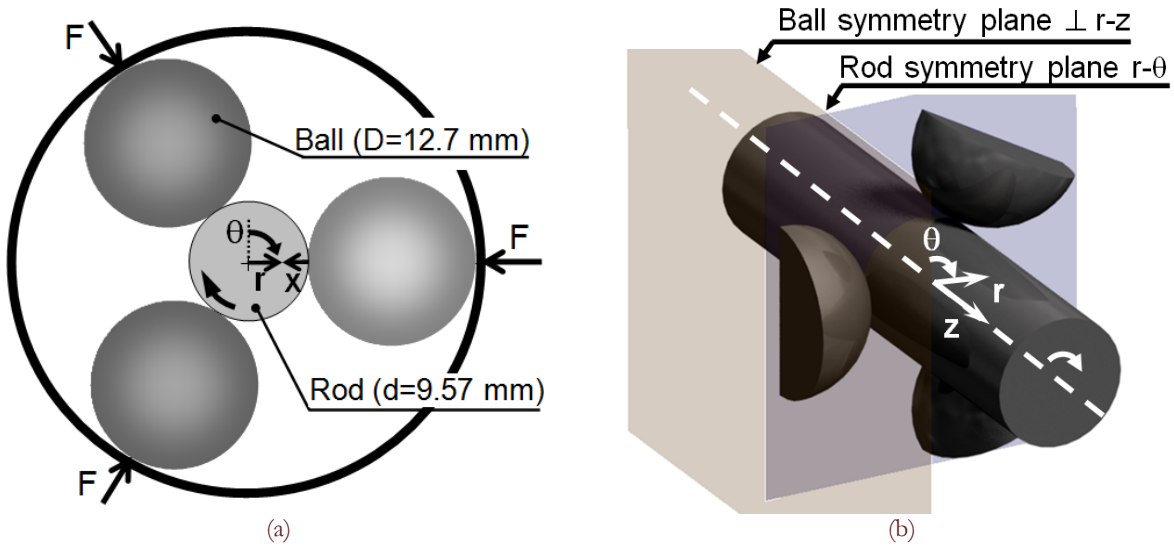


Figure 1: (a) Scheme of analysed geometry for a ball on rod test and (b) 3D geometry.

The numerical modelling of the ball-on-rod test (six revolutions) was carried out considering the material constitutive law to be elastic perfectly plastic corresponding to a steel with the following material properties for both, rod and balls: Young modulus, $E$ = 206 GPa, Poisson coefficient, ν= 0.3 and material yield stress $\sigma_Y$ = 2065 MPa. The analysis was carried out considering the isotropic strain hardening of the material and updated Lagrange procedure. According to the Hertz theory considering only the elastic response of the components [16], a very localized effect can be expected in the contact zone between rod and balls. According to this, a ball pressuring a cylinder must undergo a contact pressure of 5.5 GPa with a elliptic contacting zone whose axis length are 160 μm and 231 μm respectively.
A very refined mesh is required near the rod surface, whereas a coarser mesh was considered out of such a zone since the local effect of contact vanishes at the rod core. Thus, elements were homogenously distributed over a depth from the rod surface about 1 mm. This way, in this refined zone, the size of these elements is 43 x 52 x 280 μm in the radial, circumferential and axial directions. Regarding the meshing of the balls, the same type of elements was used, assuming a refined zone at the contact zone with element sizes similar to those used for the cylindrical bar. A point load of 300 N was placed at each ball centre and was progressively applied during the first rotation of the rod. Taking this into account, diverse meshes with linear hexaedric element of 8 nodes were considered until the required convergence on results was achieved. The optimum mesh (Fig. 2) consists in 154000 elements: 130000 for meshing the rod and 24000 for meshing the three balls.
From results of the mechanical simulation, a simple estimation of the behaviour against HA-RC-MF of the bar can be carried out considering that hydrogen diffusion proceeds from the bar surface to inner points as a function of the gradients of both hydrostatic stress (σ) and hydrogen solubility ($K_{s\varepsilon}$) [17-19]:

$$\mathbf{J} = -D(\bar{\varepsilon}_{\mathrm{p}})\left\{\nabla C - C\left[\frac{V_{\mathrm{H}}}{RT}\nabla\sigma + \frac{\nabla K_{S\varepsilon}(\bar{\varepsilon}_{\mathrm{p}})}{K_{S\varepsilon}(\bar{\varepsilon}_{\mathrm{p}})}\right]\right\} \quad (1)$$

$R$ being the universal gases constant, $V_{\mathrm{H}}$ the partial volume of hydrogen, $T$ the absolute temperature, $C$ the hydrogen concentration and $K_{S\varepsilon}$ the hydrogen solubility that is itself a one-to-one monotonic increasing function of equivalent plastic strain, as explained in detail elsewhere [17-19]. In particular, a linear relationship between plastic strain and solubility in the form $K_{S\varepsilon} = 1+4\varepsilon_{\mathrm{p}}$ was considered [17-19].

After using the matter conservation law and applying the Gauss-Ostrogradsky, the following second-order partial differential equation of hydrogen diffusion is obtained:

$$\frac{\partial C}{\partial t} = \nabla\cdot\left[D\nabla C - DC\left(\frac{V_{\mathrm{H}}}{RT}\nabla\sigma + \frac{\nabla K_{S\varepsilon}(\bar{\varepsilon}_{\mathrm{p}})}{K_{S\varepsilon}(\bar{\varepsilon}_{\mathrm{p}})}\right)\right] \quad (2)$$

The equilibrium concentration of hydrogen for infinite time of exposure to harsh environment is the steady-state solution of the differential equation. It takes the form of a Maxwell-Boltzman distribution as follows:

$$C_{\mathrm{eq}} = C_0 K_{S\varepsilon}(\bar{\varepsilon}_{\mathrm{p}})\exp\left[\frac{V_{\mathrm{H}}}{RT}\nabla\sigma\right] \quad (3)$$

where $C_0$ is the equilibrium hydrogen concentration for the material free of stress and strain. According to previous equations, hydrogen diffusion is driven by: (i) the negative gradient of hydrogen concentration (in the classical Fick´s sense); (ii) the positive gradient of hydrostatic stress; (iii) the positive gradient of hydrogen solubility, the latter is one-to-one related to the gradient of equivalent plastic strain so that the plastic strain gradient can be analysed instead of the hydrogen solubility gradient.

## MECHANICAL ANALYSIS: STRESS AND STRAIN

Numerical simulation allows the determination of the stress and strain state under cycling loading during the ball-on-rod test. During rolling, the amplitude of the fatigue loading is progressively decreasing as the depth increases, reaching an almost uniform stress evolution near the rod core. So, only points placed close to the contact will undergo real fatigue. After the fatigue loading, a multiaxial stress state appears at the rod. Thus, Figs. 2a, 3a and 4a shows the global view of the distribution of radial, hoop and axial stress respectively in the steel rod at the end of the sixth cycle, thereby after passing 17 contacting balls. For a more detailed analysis, the radial distribution of aforesaid variables are represented in Figs. 2b, 3b and 4b for different values of the hoop coordinate θ considering the following sections: (i) θ = 0º representing the contact plane between one of the balls and the rod, (ii) θ = 20º, (iii) θ = 40º, and finaly (vi) θ = 60º (corresponding to the symmetry plane between two contacting balls).

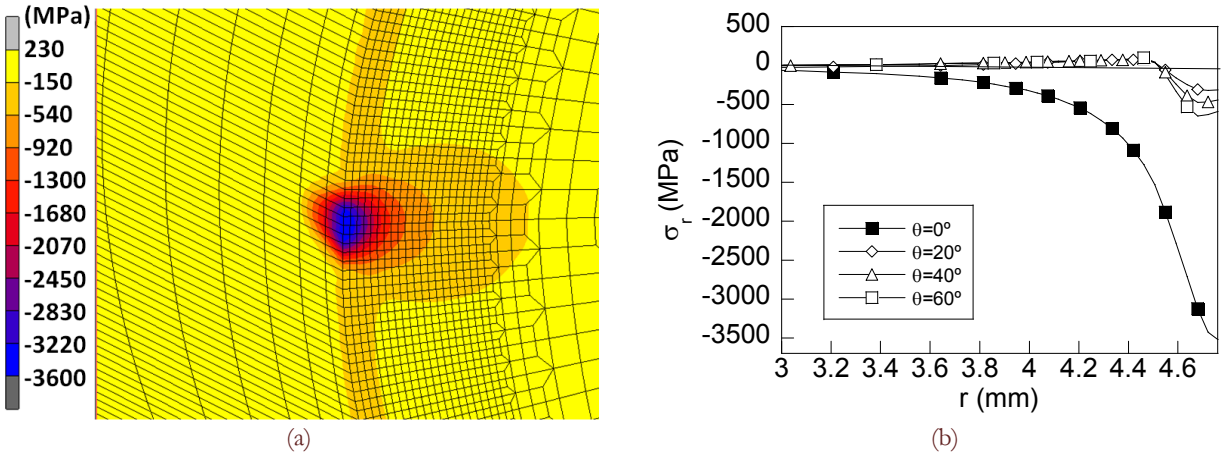


(a) (b)

Figure 2: Distribution of radial stress after the sixth loading cycle: (a) 3D view at the contact of one of the balls and (b) radial distribution for diverse hoop coordinates θ.

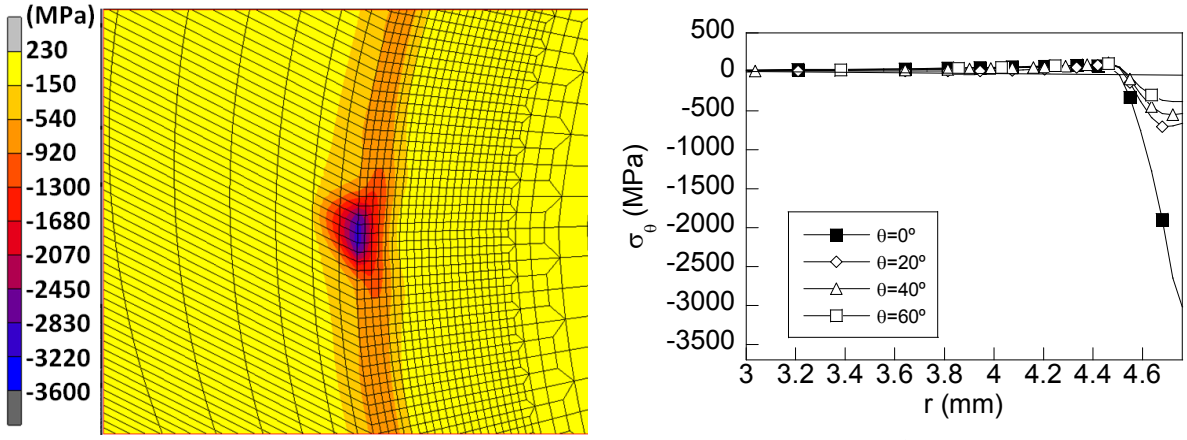


(a) (b)

Figure 3: Distribution of hoop stress after the sixth loading cycle: (a) 3D view at the contact of one of the balls and (b) radial distribution for diverse hoop coordinates θ.

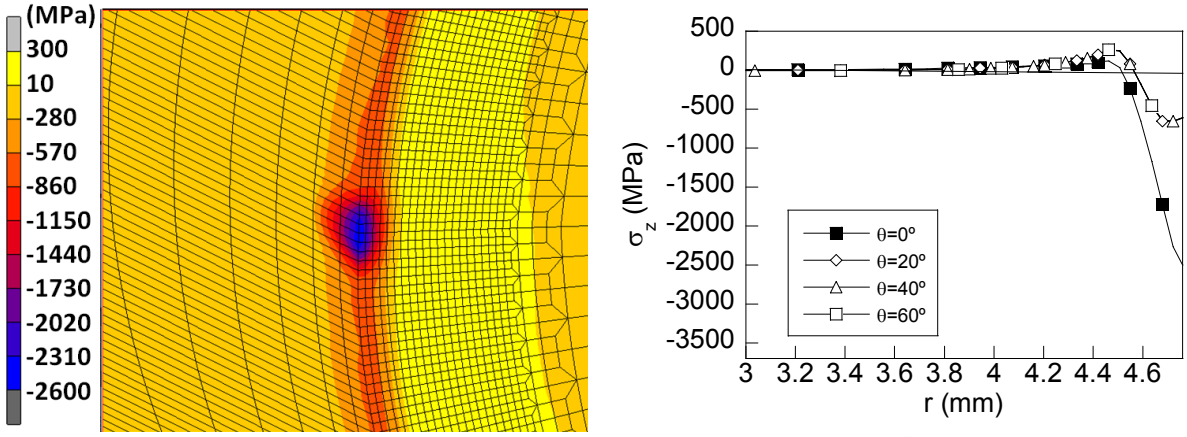


(a) (b)

Figure 4: Distribution of axial stress after the sixth loading cycle: (a) 3D view at the contact of one of the balls and (b) radial distribution for diverse hoop coordinates θ.

Results shown in Figs. 2a-4a, reveal a heavy multiaxial stress concentration localized at the contacting zones of each ball with the rolling rod. This effect progressively vanishes as the distance from the contact zone increases. Outside of the local affected zone, the stress state is homogenously distributed with a stress concentration ring located at the vicinity of the rod surface. The radial distributions shown in Figs. 2b-4b reveal a huge compressive stress at the contact radius (θ = 0º) in the radial direction caused by the pressure applied by the ball. This stress concentration is more intense for the radial stress than for the other components of the stress tensor. In addition, the extension of the local effect of contacting balls spreads through a deeper zone (around 1.5 mm) for the radial stress (Fig. 2) than those corresponding to the hoop and axial stress (around 200 μm). The extension and the maximum value of the compressive state is notably reduced at planes placed outside the contacting planes (i.e. for θ > 0º) with slight variations for hoop coordinates higher than 20º. The distributions of the hoop and axial stresses show the same high reduction of the magnitude of the stress state but, in these cases, without significant changes in the extension of the affected zone. The distribution for the other radius in contact with the other balls (θ = 120º and θ = 240º) is equivalent to that shown in Figs. 2b-4b.

Within the stress concentration zone, the values of the von Mises stress reach the material yield strength; it implies the appearance of plastic strains near the rod skin, as revealed in previous studies [2,3]. As a consequence of the values of the stress state at the rod surface vicinity, plastic strains are distributed through such a zone. Fig. 5a shows the 3D view of the field of equivalent (cumulative) plastic strain after the six cycles of the test was completed and the radial distribution of such a variable is plotted in Fig. 5b. In the same way, Fig. 6a shows the 3D view of the field of hydrostatic stress after the sixth cycle of the test was completed and Fig. 6b shows the radial distribution of such a variable for diverse values of θ.

According to this, plastic strains are distributed only over a plastic zone with ring shape spreading over 315 μm from the periphery of the rod, as shown in the same radial distribution of plastic strain obtained for diverse radial planes (different θ angles, cf. Fig. 5b) even for those closest to the contacting plane (θ = 0º). This is due to the fact that plastic strains are only generated at the contacting plane. Outside of this zone, the von Mises stress is always lower than the material yield strength and consequently no plastic strain are generated in this region. Thus, the plastic strain remains the same in all sections of the rod. A progressive decreasing distribution is obtained with a small *plateau* close to the rod cylindrical surface of 50 μm width.

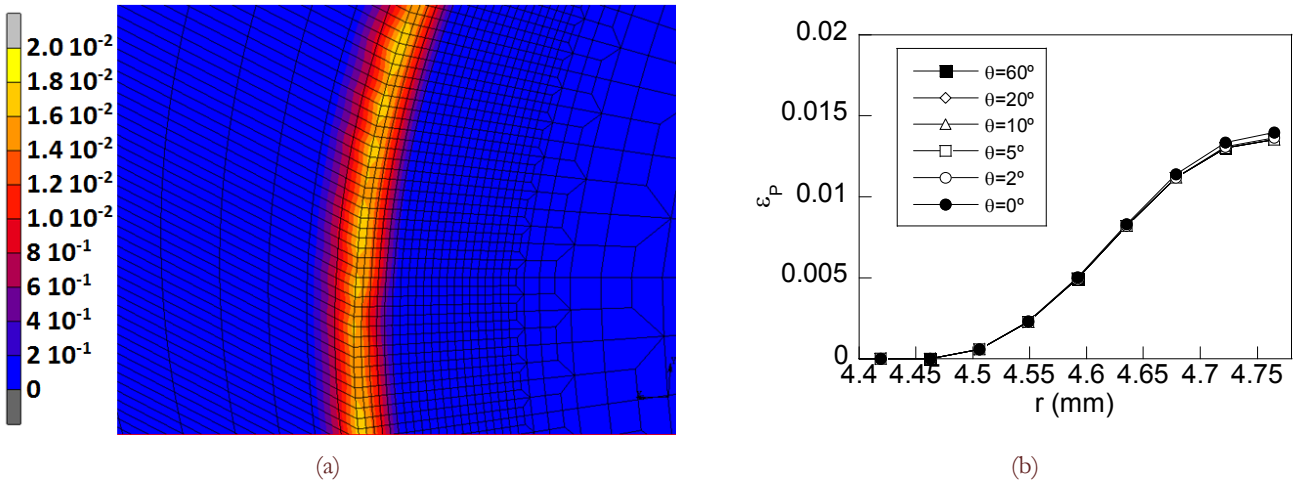


(a) (b)

Figure 5: Distribution of equivalent plastic strain after the sixth loading cycle: (a) 3D view at the contact of one of the balls and (b) radial distribution for diverse hoop coordinates θ.

The first driving force for hydrogen diffusion, the inwards gradient of equivalent plastic strains, is negative and only affects the plastic strain ring near to the rod surface (Fig. 5). With regard to the second driving force for hydrogen diffusion, the gradient of hydrostatic stress, at the contact plane (θ = 0º), a distribution of compressive nature in radial direction of such a variable is obtained, it progressively decreasing with depth up to becoming null for a depth from the rod surface of about 1 mm (Fig. 6b).

Outside the contact plane the hydrostatic stress distribution is notably reduced, so that, for angles θ higher than 20º, it is almost independent of such an angle (as it happened with the distributions of radial, hoop and axial stresses). The typical profile consist of compressive stresses over 200 μm, tensile stresses for deeper points, and, in the case of radial coordinate lower than 4 mm, a null value for hydrostatic stress is obtained.

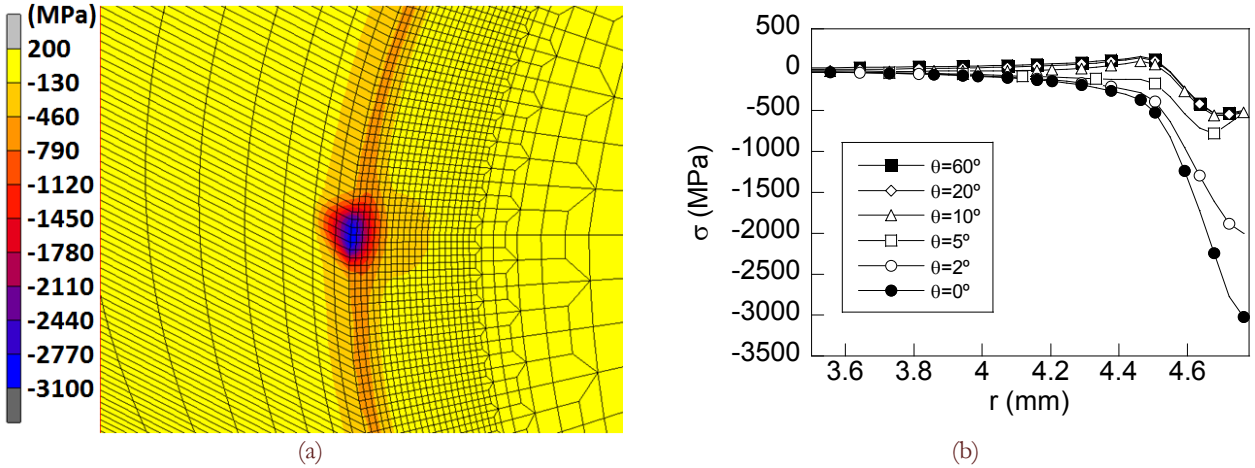


(a) (b)

Figure 6: Distribution of hydrostatic stress: (a) 3D view of the contacting plane and (b) radial distribution for diverse circumferential coordinate θ.

For completing the analysis of hydrogen diffusion and accumulation on the rod during life in service, the information obtained from the estimation of hydrogen concentration in the radial direction [2,3] can be completed by a discussion of the implications of diffusion in the circumferential direction. To do so, the circumferential distribution of the variables affecting the hydrogen diffusion assisted by stress and strain is plotted in Fig. 5, considering diverse layers within the plastic zone.

The circumferential distribution of hydrostatic stress shown in Fig. 7a reveals a local stress concentration in the vicinity of the contacting plane $\theta = 0^{\circ}$ where the maximum hydrostatic stress is placed. Within a range of planes around 5º, the hydrostatic stress progressively decreases, becoming almost constant for other values of θ. This behaviour is observed for the distributions corresponding to depths around half size of the plastic zone (173 μm approximately) with compressive stresses out of the affected zone.

As the depth from the rod surface increases, the maximum value of the stress is suddenly decreased (a 90% for the depth around the size of the plastic zone $x = 300$ μm, a 60% for the depth around half size of the plastic zone $x = 173$ μm and a 25% just for a depth of 86 μm). Beyond this depth the stress continuously decreases up to becoming almost null for deeper points. This way, in hoop direction hydrogen will be pumped out of the contact plane by means of a huge gradient of plastic strains.

With regard to circumferential plastic strains, a minimum is placed close to the contact section ($\theta = 0^{\circ}$) where a slight local maximum appears, thereby creating a gradient of plastic strains. This gradient drives hydrogen out of the contact plane to planes with a higher θ. This effect is vanished with depth resulting almost null for depths from surface of 216 μm and null for depths from the rod surface out of the plastic zone ($x > 315$ μm) observed in Fig. 5. Plastic strain slowly increases with the hoop coordinate θ, reaching a maximum value at $\theta = 45^{\circ}$. So, hydrogen will be pumped out suddenly from the contact plane and lately is dragged slowly for points placed at higher hoop coordinates (due to slower gradient far from the contact plane).

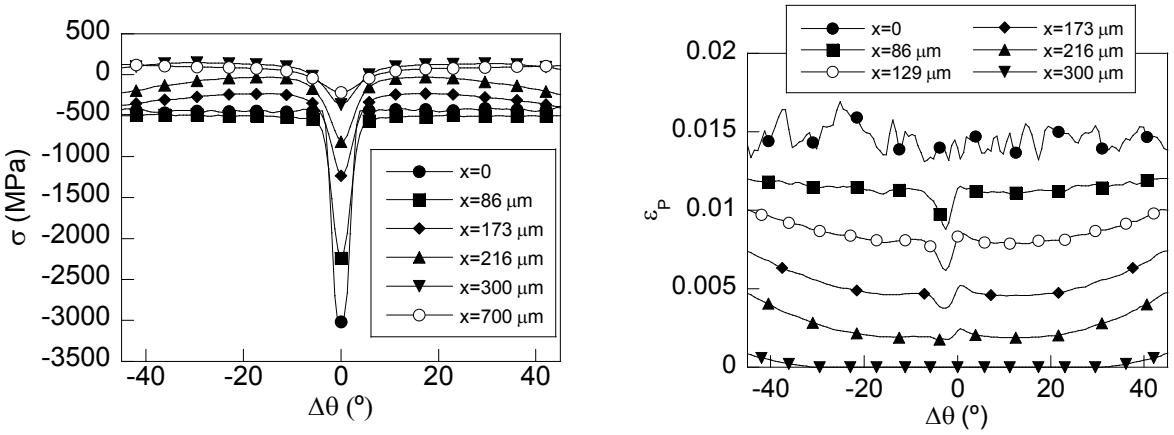


(a) (b)

Figure 7: Circumferential distribution of (a) hydrostatic stress and (b) equivalent plastic strain at diverse layers of the rod between the contacting balls.

Finally, Fig. 8 shows the axial distribution of both hydrostatic stress and equivalent plastic strain for diverse values of depth from the rod surface ($x$). In the axial direction, a very located distribution of both hydrostatic stress and plastic strains near to contact plane is obtained. With regard to the hydrostatic stress distribution, the high compressive stress at the contact plane is progressively decreased as the distance from the contact plane ($z$) is increased, obtaining a null distribution of such a variable for $z > 1.5$ mm.

As the depth from the rod surface increases, the hydrostatic stress at the contacting plane ($z = 0$ mm) progressively decreases and, consequently, the inwards gradient of hydrostatic stress in the axial direction is reduced as the depth from the rod surface is increased. Thus, hydrogen placed close to the contact between ball and bar is also pumped in the axial direction due to the positive inwards gradient of hydrostatic stress. This effect is progressively reduced with the depth $x$ becoming almost negligible for depths $x > 600$ μm. Finally, the axial distribution of plastic strains appears through a narrow zone becoming null for axial distances $z > 500$ μm.

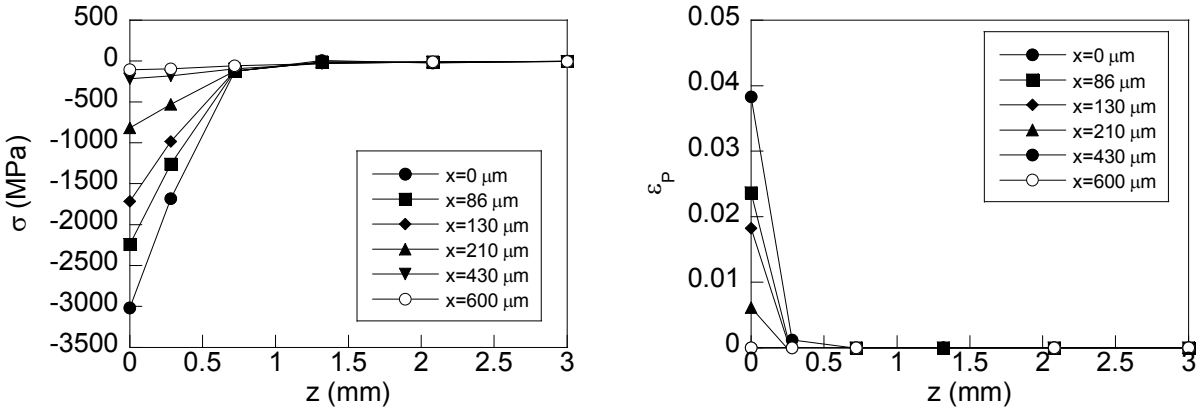


(a) (b)

Figure 8: Axial distribution of hydrostatic stress for diverse depths ($x$): (a) general plot and (b) detail plot near the rod surface (zone with strong gradients).

As in the case of the hydrostatic stress distribution, the plastic strain at the contact plane ($z$ = 0 mm) decreases with depth from the rod surface ($x$), and consequently the inwards gradient is progressively reduced as the variable $x$ is increased becoming null for depths $x$ > 600 μm. However, the inwards gradient of equivalent plastic strains is negative, thereby; the hydrogen diffusion is not enhanced. This opposition is progressively annulled as the depth from rod surface is increased. So, two competitive factors are involved in the diffusion of hydrogen placed near to the contact between ball and bar. On one hand, the inwards gradient of hydrostatic stress enhances the diffusion of hydrogen out of the contact plane whereas; on the other hand, the inwards gradient of equivalent plastic strains is opposite, impeding the aforesaid diffusion. This effect is only noticeable near the contact zone and, therefore, the diffusion of hydrogen placed at deeper points ($x$ > 600 μm) can be considered only driven by the gradient of hydrogen concentration in axial direction.

## CHEMICAL ANALYSIS: HYDROGEN TRANSPORT BY DIFFUSION

For assessing the HA-RC-MF behaviour of the rolling rod, it is interesting to analyse the long-time behaviour of the component under hydrogen exposure. To this end, the steady state distribution of hydrogen concentration through the rod radius was obtained (Fig. 9) using eq. (3) and taking into account both hydrostatic stress and equivalent plastic strain. Plot is associated with infinite time (steady state solution from the mathematical point of view) or with thermodynamical equilibrium of the hydrogen-metal system (from the physical view point).

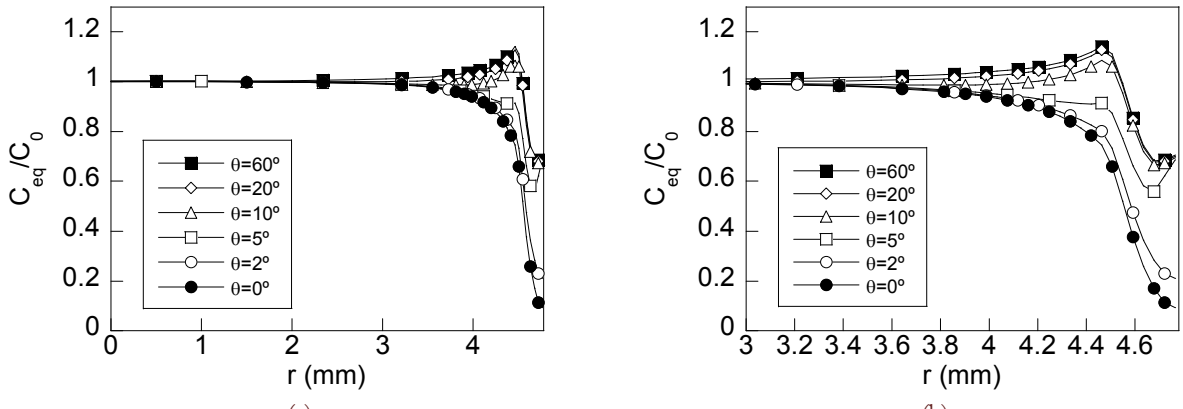


(a) (b)

Figure 9: Radial distribution of the hydrogen concentration for diverse circumferential coordinate θ: (a) general plot and (b) detail plot near the rod surface.

The discussion about HA-RC-MF is focused in the quantitative analysis of the hydrogen amount in radial, hoop and axial directions by applying the steady-state solution of the diffusion equation shown in eq. (3) to the distributions of the components of the stress tensor and plastic strain shown in Figs. 2 and 4 respectively. Thus, Fig. 9 shows the radial laws of hydrogen concentration along diverse radial planes considering the stress and strain states shown in Figs. 5 and 6, whereas Figs. 10 and 11 shows the distribution of hydrogen concentration in the hoop and axial directions respectively.
According to these results, for long time of exposure to the hydrogenating environment, the hydrogen amount at the rod surface vicinity (within the stress and strain affected zone of the rod, i.e., for depths from the rod surface lower than 1 mm) is progressively increased with the circumferential distance to the contacting ball. Thus, for the plane where the ball is contacting the rod, a huge reduction of the hydrogen amount is observed due to the high compressive stresses produced by the contact pressure (Fig. 6). Consequently, hydrogen diffusion is promoted out of the contact affected zone due to the gradient of both driving forces for hydrogen diffusion: the inwards gradient of plastic strain and the inwards gradient of hydrostatic stress.
This effect is also progressively vanished as the distance from the contact plane increases, it being noticeable for planes very close to the contact plane where an important reduction of the hydrogen concentration is also achieved. Nevertheless, for planes with circumferential coordinates higher than 10º from the contact plane, the hydrogen amount at surface is similar than that obtained for higher angle θ. The distributions of hydrogen for planes with circumferential coordinate higher than 10º just exhibit slight changes.
An interesting issue is observed for these planes from the point of view of HA-RC-MF. At the rod surface vicinity over a depth of 200 μm a significant reduction is observed due to the compressive stresses (Fig. 6) with a small *plateau* of 50 μm. Hereafter the hydrogen concentration increases with depth, reaching the maximum value ($C/C_0$ = 1.15) of the distribution for a depth of 300 μm and for deeper points softly decreases up to the rod core where the concentration associated with thermo-dynamical equilibrium of the material free of stress and strain ($C_0$) is achieved. So, the potential place of damage would be placed through a zone extended between the balls for depth from surface of 300 μm.
The hoop distribution of hydrogen for long times of exposure to the hydrogenating environment is presented in Fig. 10, where different depth layers (diverse depths) are depicted, considering the stress and strain states obtained from numerical simulation (Fig. 8).

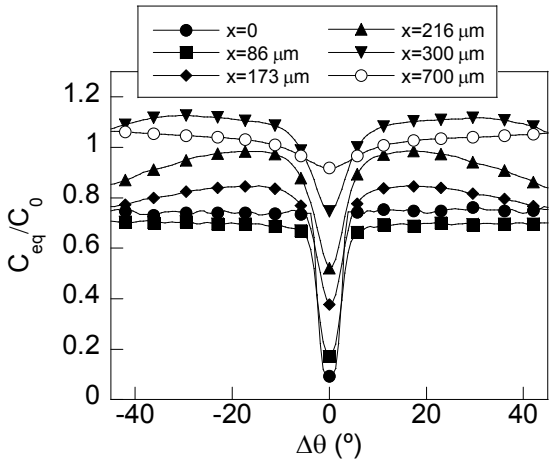


Figure 10: Hydrogen distribution for long times of diffusion in the circumferential direction at diverse layers of the rod between the contacting balls.

Regarding the hoop distribution of hydrogen concentration shown in Fig. 10, the hydrogen accumulation is placed out of the contacting plane (θ = 0º) and surrounding planes where a huge reduction of the hydrogen amount is observed. This reduction becomes lower as the depth from the surface is increased. Out of this zone hydrogen is uniformly distributed for depths up to 86 μm. For distribution obtained at higher depths, hydrogen is progressively increased for θ > 5º, reaching a maximum hydrogen concentration at θ = 20º and, hereafter, decreasing slowly.
The aforesaid trend is repeated at deeper layers, increasing the maximum hydrogen amount zone as the depth increases (according to the distributions of hydrostatic stress shown in Fig. 6a). For layers placed far from the contact, hydrogen is almost uniformly distributed in the hoop direction, reaching a maximum hydrogen concentration, $C/C_0$ = 1.13, for a

depth 300 μm. Hereafter, the hydrogen distribution is progressively decreased, approaching the equilibrium hydrogen concentration for the material free of stress and strain ($C_{eq}/C_0$ = 1). So, the maximum hydrogen amount is placed out of the contact plane at a depth from the rod surface of 300 μm.

To conclude the analysis, the hydrogen distribution in the axial direction is presented in Fig. 11 for diverse depths within the plastic strain affected zone observed previously in Fig. 5. Thus, the hydrogen concentration is highly decreased at the vicinity of the contact zone (0 < z < 1.2 mm). So, the shorter the distance from the contact area, the lower the reduction of hydrogen amount. Thus, for a depth of 700 μm, the distribution of hydrogen is rather affected by the stress and strain states generated by HA-RC-MF.

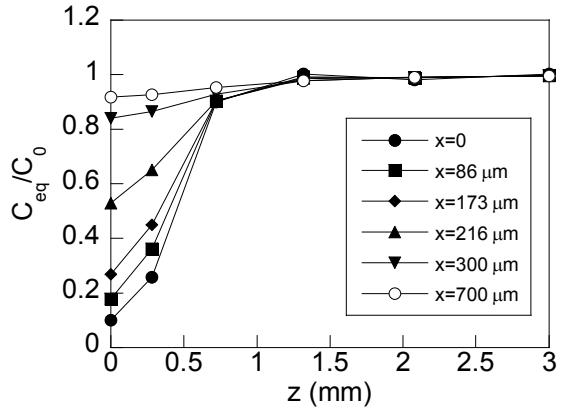


Figure 11: Hydrogen distribution for long times of diffusion in the axial direction at diverse layers of the rod between the contacting balls.

## Conclusions

In a ball-on-rod test, non-uniform plastic strains are generated on the contact plane where the ball applies a huge pressure to the rod overcoming material yield strength. This state is located near the rod surface with a plastic zone spreading over a maximum depth of 300 μm. A huge compressive stress appears in the vicinity of the rod surface; it is progressively reduced as the distance from the surface increases in radial, hoop and axial directions. As a result, hydrogen is accumulated out of the contact plane where a huge reduction of the hydrogen amount is achieved for long times of exposure to the environment due to the high compressive hydrostatic stress in the radial direction, thereby pumping hydrogen towards points outside the contact plane. The maximum hydrogen amount appears for a depth from the surface about 300 μm at planes placed 20º out of the contact plane in the contact cross section of the bar.

## Acknowledgements

The authors acknowledge the financial support provided by the EU Project **MultiHy** (http://multihy.eu): Multiscale modelling of hydrogen embrittlement of crystalline materials (EU-FP7-NMP Project No. 263335).

## References

[1] Europe's onshore and offshore wind energy potential: an assessment of environmental and economic constraints. European Environment Agency, Copenhagen, (2009).

[2] Toribio, J., Lorenzo, M., Vergara, D., Kharin, V., Hydrogen-assisted rolling-contact fatigue of wind turbines bearings. Key Eng. Mater., 627 (2015) 157–160.

[3] Toribio, J., Lorenzo, M., Vergara, D., Kharin, V., Numerical analysis of hydrogen-assisted rolling-contact fatigue of wind turbine bearings. Frattura ed Integrità Strutturale, 30 (2014) 40–47.

[4] Kumar, A., Hahn, G., Rubin, D., A study of subsurface crack initiation produced by rolling contact fatigue, Metall. Trans. A, 24 (1993) 351–359.
[5] Bhargava, V., Hahn, G. T., Rubin, C. A., Rolling contact deformation and microstructural changes in high strength bearing steel, Wear, 133 (1989) 65–71.
[6] Gupta, V., Bastias, P., Hahn, G. T., Rubin, C. A., Elasto-plastic finite-element analysis of 2-D rolling-plus-sliding contact with temperature-dependent bearing steel material properties, Wear, 169 (1993) 251–256.
[7] Jiang, Y., Su, B., Sehitoglu, H., Three-dimensional elastic-plastic stress analysis of rolling contact, J. Tribol., 124 (2002) 699–708.
[8] Kabo, E., Ekberg, A., Fatigue initiation in railway wheels—a numerical study of the influence of defects, Wear, 253 (2002) 26–34.
[9] Kabo, E., Ekberg, A., Material defects in rolling contact fatigue of railway wheels—the influence of defect size, Wear, 258 (2005) 1194–1200.
[10] Rider, R. J., Harvey, S. J., Chandler, H. D., Fatigue and ratcheting interactions, Inter. J. Fatigue, 17 (1995) 507–511.
[11] Lim, C. B., Kim, K. S., Seong, J. B., Ratcheting and fatigue behavior of a copper alloy under uniaxial cyclic loading with mean stress, Inter. J. Fatigue, 31 (2009) 501–507.
[12] Pandkar, A. S., Arakere, N., Subhash, G., Microstructure-sensitive accumulation of plastic strain due to ratcheting in bearing steels subject to rolling fatigue, Inter. J. Fatigue, 63 (2014) 191–202.
[13] Glover, D. A ball-rod rolling contact fatigue tester, in: Rolling contact fatigue testing of bearing steels. ASTM STP 771, American Society for Testing and Materials, Baltimore, MD, (1982) 107–124.
[14] Bhattacharyya, A., Subhash, G., Arakere, N., Evolution of subsurface plastic zone due to rolling contact fatigue of M-50 NiL case hardened bearing steel, Inter. J. Fatigue, 59 (2014) 102–113.
[15] Arakere, N. K., Subhash, G., Work hardening response of M50-NiL case hardened bearing steel during shakedown in rolling contact fatigue, Mater. Sci. Tech., 28 (2012) 34–38.
[16] Pilkey, W. D., Formulas for stress, strain, and structural matrices, Second ed., John Wiley & Sons, Inc., Hoboken, NJ, USA, (2008).
[17] Toribio, J., Lorenzo, M., Vergara, D., Kharin, V., Hydrogen degradation of cold-drawn wires: a numerical analysis of drawing-induced residual stresses and strains, Corros., 67 (2011) 075001–075008.
[18] Toribio, J., Kharin, V., Lorenzo, M., Vergara, D., Role of drawing-induced residual stresses and strains in the hydrogen embrittlement susceptibility of prestressing steels, Corros. Sci., 53 (2011) 3346–3355.
[19] Toribio, J., Kharin, V., Vergara, D., Lorenzo, M., Two-dimensional numerical modelling of hydrogen diffusion in metals assisted by both stress and strain, Adv. Mater. Res., 138 (2010) 117–126.